Correlations Between the Thermosphere's Semiannual Density Variations and Infrared Emissions Measured With the SABER Instrument

Weimer, D. R.; Mlynczak, M. G.; Emmert, J. T.; Doornbos, E.; Sutton, E. K.; Hunt, L. A.

Important note
To cite this publication, please use the final published version (if applicable).
Please check the document version above.

RESEARCH ARTICLE

Correspondence to:
D. R. Weimer,
dweimer@vt.edu

Correlations Between the Thermosphere's Semiannual Density Variations and Infrared Emissions Measured With the SABER Instrument

D. R. Weimer[1,2] (ID), **M. G. Mlynczak**[3] (ID), **J. T. Emmert**[4] (ID), **E. Doornbos**[5] (ID), **E. K. Sutton**[6] (ID), and **L. A. Hunt**[7] (ID)

[1]Center for Space Science and Engineering Research, Virginia Tech, Blacksburg, VA, USA, [2]National Institute of Aerospace, Hampton, VA, USA, [3]Science Directorate, NASA Langley Research Center, Hampton, VA, USA, [4]Space Science Division, U.S. Naval Research Laboratory, DC, Washington, USA, [5]Faculty of Aerospace Engineering, Delft University of Technology, Delft, Netherlands, [6]Space Weather Technology, Research, and Education Center, University of Colorado Boulder, Boulder, CO, USA, [7]Science Systems and Applications, Inc., Hampton, VA, USA

Abstract This paper presents measurements of the amplitudes and timings of the combined, annual, and semiannual variations of thermospheric neutral density, and a comparison of these density variations with measurements of the infrared emissions from carbon dioxide and nitric oxide in the thermosphere. The density values were obtained from measurements of the atmospheric drag experienced by the Challenging Minisatellite Payload, Gravity Recovery and Climate Experiment A, Gravity field and Ocean Circulation Explorer, and three Swarm satellites, while the optical emissions were measured with the Sounding of the Atmosphere using Broadband Emission Radiometry (SABER) instrument on the Thermosphere Ionosphere Mesosphere Energetics and Dynamics satellite. These data span a time period of 16 years. A database containing global average densities that were derived from the orbits of about 5,000 objects (Emmert, 2009, https://doi.org/10.1029/2009JA014102, 2015b, https://doi.org/10.1002/2015JA021047) was employed for calibrating these density data. A comparison with the NRLMSISE-00 model was used to derive measurements of how much the density changes over time due to these seasonal variations. It is found that the seasonal density oscillations have significant variations in amplitude and timing. In order to test the practicality of using optical emissions as a monitoring tool, the SABER data were fit to the measured variations. Even the most simple fit that used only filtered carbon dioxide emissions had good correlations with the measured oscillations. However, the density oscillations were also well predicted by a simple Fourier series, contrary to original expectations. Nevertheless, measurements of the optical emissions from the thermosphere are expected to have a role in future understanding and prediction of the semiannual variations.

Plain Language Summary The uppermost atmosphere, known as the *thermosphere*, undergoes oscillations in the density of the neutral atoms and molecules, producing two peaks and valleys in the density in each year. The timing of of these "semiannual" variations or oscillations, as well as their amplitudes, tends to vary. Their unpredictability makes it harder to accurately model the amount of drag experienced by orbiting satellites. It had been noticed that the infrared light emitted by carbon dioxide molecules in the thermosphere has a tendency to follow the semiannual oscillations. Such emissions have been measured by an instrument on a NASA satellite for the past 16 years. We have compared these emissions with the variations in the semiannual oscillations that were derived from measurements of the drag seen by six different satellites flown by both NASA and the European Space Agency during the same time period, though not at the same time. The results of the comparison show how well the infrared emissions match the density oscillations, due to changes in both the composition and temperature of the thermosphere that influence both. Results show that further study will be needed to be able to accurately predict the density oscillations.

1. Introduction

Variations in the neutral densities in the thermosphere, or upper atmosphere, have several different drivers, each producing density changes on different time scales. Changes in the level of solar radiation are a

primary driver, occurring over scales ranging from solar rotations up through the solar cycle. Solar flares produce shorter-term density fluctuations, as well as the heating in the ionosphere that results from the solar wind-magnetosphere-ionosphere interaction. Moreover, as noted by Paetzold and Zschörner (1961), the thermosphere has global-level, annual oscillations and semiannual oscillations (SAOs).

These oscillations cause density peaks in April and October, and minimums around January and July. The amplitudes and timing of these oscillations vary from year to year, so that the combined effect of the annual oscillation and SAO are difficult to accurately model or predict. While Bowman et al. (2008) had indicated that the levels of the solar ultraviolet radiation influences the SAO, the exact causes have not been known. Emmert (2015a) reviews some of the possible explanations for the oscillations.

Previously, Mlynczak et al. (2008) and Weimer et al. (2016) had found evidence that the carbon dioxide (CO_2) emissions measured with the Sounding of the Atmosphere using Broadband Emission Radiometry (SABER) instrument on the Thermosphere Ionosphere Mesosphere Energetics and Dynamics (TIMED) spacecraft had a correlation with the SAO in the thermosphere. The given explanation was that the variations in the thermosphere's density resulted from changes in the level of atomic oxygen and that the variations in the CO_2 emissions resulted from collisions between atomic oxygen and CO_2. Additionally, variations in the CO_2 amounts likely have annual oscillations and SAOs since the CO2 is not well mixed in the upper mesosphere and lower thermosphere (Mlynczak et al., 2010).

More recently, Jones et al. (2018) had probed the causes of the SAO through use of the National Center for Atmospheric Research thermosphere-ionosphere-mesosphere-electrodynamics general circulation model, showing that Earth's obliquity generates the density oscillations through changes in the large-scale transport of neutral thermospheric constituents. Jones et al. (2018) findings support the claim of Fuller-Rowell (1998) that the "thermospheric spoon" mechanism drives stronger interhemispheric transport during solstice (see Sutton, 2016).

The objective of this paper is to examine the characteristics of the SAO in greater detail and to determine whether or not measurements of the infrared emissions from CO_2 and nitric oxide (NO) could, in principle, be used for real-time monitoring of the state of these thermospheric oscillations. Since the SAO variations tend to have variability that cannot be predicted with great precision by models, could remote sensing be useful for "nowcasts" of thermospheric densities? The investigation techniques used in the present paper go several steps beyond the methods shown by Weimer et al. (2016). One step taken is to use additional measurements of thermospheric neutral density to extend the time series by several years. The approach used to cross-check the density measurements has also been refined. Finally, a more detailed analysis is applied to the correlations between the SAOs and the infrared emissions detected with the SABER instrument.

2. Resources

2.1. Infrared Emissions Measured With the SABER
Measurements of infrared emissions from the thermosphere taken by the SABER instrument on the TIMED spacecraft (Mlynczak et al., 2005, 2010) are used extensively in this work. Figure 1 shows SABER measurements of the NO and CO_2 emissions, for the years 2002 through 2017. The thin green and brown lines show the daily mean power of the NO and CO_2 emissions, in units of gigawatts (GW). The thick lines having similar colors show the result of smoothing with a 31-day moving average. Superposed over these graphs are the same data after smoothing with a yearly average, shown in black.

Right away, it is evident from Figure 1 that the thick brown line, showing the filtered CO_2 emissions, has periodic variations that tend to match the annual and semiannual variations in the thermosphere, as found earlier by Mlynczak et al. (2008). The extent of this agreement will be analyzed in greater detail later in this paper.

2.2. Satellite Neutral Density Measurements
The prior publication by Weimer et al. (2016) had used neutral density data from the Challenging Minisatellite Payload (CHAMP) and Gravity Recovery and Climate Experiment (GRACE) satellites (Bruinsma et al., 2004; Tapley et al., 2004). The CHAMP data had spanned the years 2002 through 2008, and the GRACE data had covered the years 2003 through 2009. For the results presented here, the CHAMP data now include an additional year, through 2009, and the GRACE data are extended through the end of 2010, with a gap in part of the last year. The source of these density data has changed as well, now with better temporal and spatial resolution
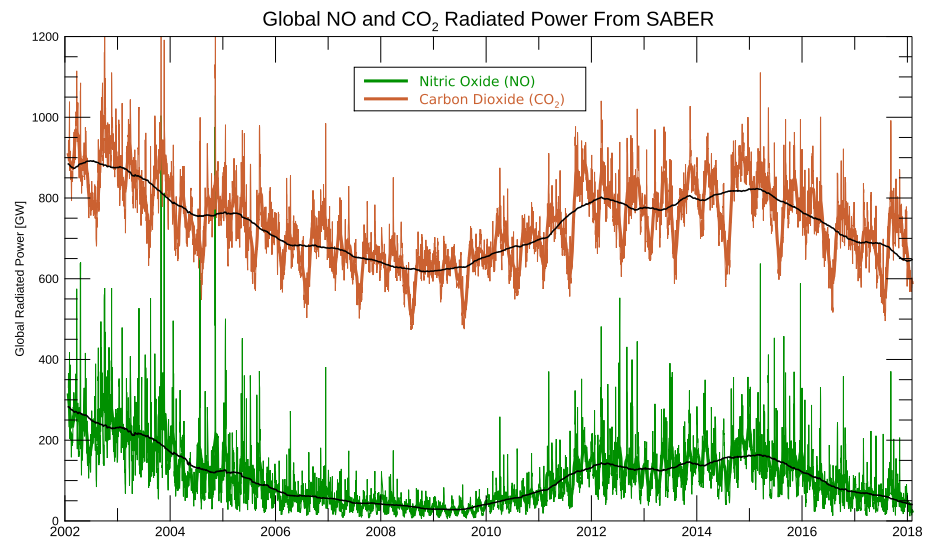
Figure 1. Global totals of nitric oxide (NO) and carbon dioxide (CO_2) emissions measured by the SABER instrument. The thin green and brown lines show the daily mean power, in gigawatts, for NO and CO_2, respectively. The thicker lines having similar colors show the same data after smoothing with a moving average of 31 days. The superposed, black lines show the result of similar smoothing with a yearly average. SABER = Sounding of the Atmosphere using Broadband Emission Radiometry.

(from http://tinyurl.com/RSM-Models; Mehta et al., 2017). These data files include two different versions of the neutral densities, and the densities by Piyush Mehta are used here.

Additional data from two newer missions have also been added, extending the time series of the density data up to the end of 2017. These additional data include neutral density measurements from the European Space Agency's Gravity field and Ocean Circulation Explorer (GOCE; Doornbos et al., 2014; Doornbos, 2016), covering late 2009 through most of 2013. Version 1.5 of these data are used in this study. The other data are from the European Space Agency's Swarm mission, which consists of a constellation of three identical satellites (Swarms A, B, and C) that were launched on 22 November 2013 (Haagmans et al., 2013). Swarms A and C spacecraft orbit at an altitude of approximately 470 km, separated by about 1.4° in longitude, while B has a higher altitude, at about 520 km. The neutral density data from the Swarm spacecraft that are used here span a little over 4 years, from 30 November 2013 to the end of 2017. One unique aspect of these data is that, rather than being derived from a conventional accelerometer instrument, these density data are based on calculation from precise orbit determinations using the Global Positioning System receivers on the spacecraft. While the Swarm spacecraft do carry accelerometers, it was found that their output contain many anomalies, so this alternative technique was developed. These Global Positioning System-derived densities are obtained from an orbit determination that uses a Kalman filter approach. While these density data have a much lower spatial resolution than can normally be obtained from accelerometers, the resolved spatial scales are sufficient for our purposes, as shown in the first published use by Astafyeva et al. (2017).

2.3. NRLMSISE-00 Thermosphere Density Model

In this work we use the Naval Research Laboratory's thermosphere density model, known as the "NRL Mass Spectrometer and Incoherent Scatter radar Extended model (NRLMSISE-00)" (Hedin, 1991; Picone et al., 2002), abbreviated herein as simply "MSIS." This model provides the density of several atomic and molecular species, as well as temperature, as a function of altitude and geographical location, using input parameters of date, time, and the solar $F_{10.7}$ index. Geomagnetic activity is another input into the model using either the daily A_p index, or optionally, several 3-hr ap indices.

2.4. Orbit-Derived Global Mean Thermosphere Density

For this research we also made extensive use of thermosphere density measurements described by Emmert, (2009, 2015b), in which neutral densities were derived, as a function of altitude between 200 and 600 km, from an analysis of the orbits of approximately 5,000 objects, including space debris. These orbits were derived from radar tracking of the satellites and debris by the Air Force and supplied in the form of orbital elements in the standard, "two-line element" (TLE) format. Figure 2 is reproduced from Emmert (2015b), showing the
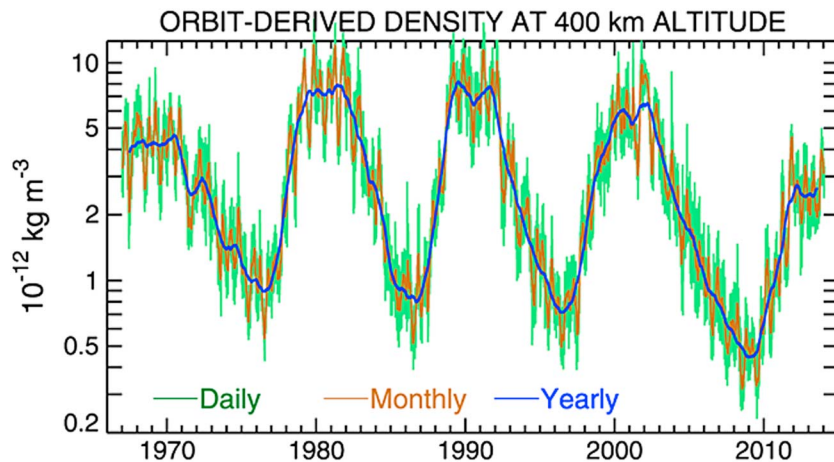
Figure 2. From Emmert (2015b), global average thermospheric mass density derived from the orbits of about 5,000 objects, obtained from orbit data from 1967 to 2013. Results are graphed for an altitude of 400 km, with the green line showing daily values, monthly running averages in orange, and yearly running averages in blue.

global average thermospheric mass densities at an altitude of 400 km. The green line in this figure shows the daily values, while monthly, running averages are drawn in orange, and yearly running averages in blue.

In the orbit-derived density method (Emmert, 2009), global average density ratios with respect to MSIS are retrieved first and then applied to the global average MSIS density to obtain the density estimates. Emmert (2015b) provided daily, 1967–2013 density values, at 10 selected altitudes between 250 and 575 km, as supporting information. Here we use the more fundamental density ratios (which we label "TLE" in the figures and which are given in the data archive indicated in the acknowledgments) for the purpose of checking the calibration of the satellite drag measurements.

All neutral density measurements that are based on satellite drag have inherent systematic uncertainties in the reference ballistic coefficients, which translate into systematic scale offsets in the densities. These uncertainties originate in the data processing due to three main reasons: (1) an incomplete representation of the satellite outer surface geometry and its orientation with respect to the flow, (2) a lack of information on the temperature and composition of the gas particles, and (3) limited information on the way in which the gas particles exchange momentum with the satellite surfaces (Doornbos, 2012). Considerable effort has been put in using high-fidelity geometry and attitude data, as well as gas-surface interaction models in the processing of densities from CHAMP, GRACE, GOCE, and Swarm. However, the highly elongated shapes of these satellites make the calculation of their ballistic coefficients especially sensitive to these uncertain factors, and therefore still considerable differences in the scale of the resulting density data sets remain. Although efforts are underway to further reduce the discrepancies between the data sets in their processing (March et al., 2018), there is currently still a need to bring the data sets of these satellites better in line. The TLE-derived densities are used here for this purpose, because they represent the global time-averaged thermosphere density variations very well. In principle, all data sets could have been adjusted towards a model, such as NRLMSISE-00, but that would have introduced time-varying model biases into the data intercalibration.

For the derivation of the TLE-derived densities, the spherical Starshine 1 satellite was used as the primary calibration object; the ballistic coefficients of the other objects were bootstrapped from there and constrained to produce mutually consistent densities. Subsequently, Pilinski et al. (2011) investigated the aerodynamic properties of Starshine 1 in more detail, including a modeling of the mirrors covering the surface and the presence of a launch ring adapter, resulting in an increased estimate of its ballistic coefficient. For the remainder of this paper, the original TLE density measurements have been multiplied by a factor of 0.93 in order to account for a revised (higher) coefficient of drag and reference area for the Starshine 1 satellite.

3. Outline of Analysis Process

As several sequential steps were required for our analysis, it is helpful to first summarize the process before getting into the detailed descriptions. An outline follows:
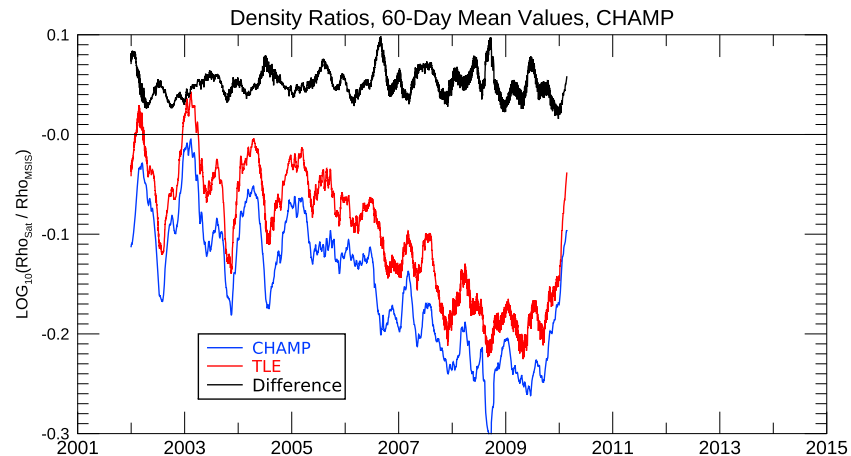
Figure 3. (blue) Natural log of the ratio of CHAMP densities with respect to MSIS. (red) Corresponding TLE log-ratios, interpolated to the altitude of CHAMP. (black) The difference between the TLE and CHAMP log-ratios. CHAMP = Challenging Minisatellite Payload; TLE = two-line element.

1. The calculations of the ballistic coefficients and the resulting density derivations are complex and prone to some uncertainties. Since density measurements from several different satellites and missions are used, in the first step their density measurements are checked to see how well they agree. Calculations from the MSIS model are compared with the measured densities. The ratios of the densities that are obtained indicate how each satellite performs relative to MSIS. As the MSIS model also has errors, particularly during solar minimum, the TLE database described in the previous section is employed to provide a standard point of reference. The results from this comparison are correction factors for the density measurements that bring the various data sets into agreement with the TLE values.

2. While the timespan of the TLE database extends through both the CHAMP, GRACE, and GOCE missions, it ends just as the Swarm mission is getting started. In order to do a calibration check on the density measurements from the Swarm satellites, the TLE values are extended in time through use of the SABER measurements of the global NO and CO_2 emissions.

3. The adjusted density measurements are again compared with the values calculated from the MSIS model at every data point, but now turning off the parameters in the MSIS model that control the annual and semi-annual variations. The resulting differences between the measured and model values are an indication of the actual variations. These differences are can be evaluated in two ways, either as the percentage change in oxygen that would account for the observed variability or as the logarithm of the ratio of measured and modeled values.

4. The measurements are processed with a digital band-pass filter that smooths out the orbital and daily variability and removes the long-term, solar cycle variations. The same filtering is applied to the SABER measurements of the the global NO and CO_2 emissions.

5. The filtered values are compared. Different formulas are tried with least-error fits to determine how well the SABER measurements match up with the semiannual thermosphere variability.

4. Calibrating the Neutral Density Measurements

Weimer et al. (2016) had previously used the MSIS model to make relative comparisons of the density measurements from the CHAMP and GRACE satellites; the densities were then adjusted in order to produce the same ratios with respect to the MSIS model. As the source of the CHAMP and GRACE densities has changed, now with improved temporal resolution, and the other satellite data are new, this calibration needed to be redone. As the satellite missions do not all overlap in time, for this work the cross-calibration of the data sets has been accomplished in a different manner.

Starting with the data from the CHAMP satellite, Figure 3 shows a comparison of density ratios, with respect to MSIS, derived from both the satellite and TLE data. The TLE ratios were interpolated to the same altitude as the CHAMP satellite at each point in time; this altitude varied from approximately 400–500 km (perigee to
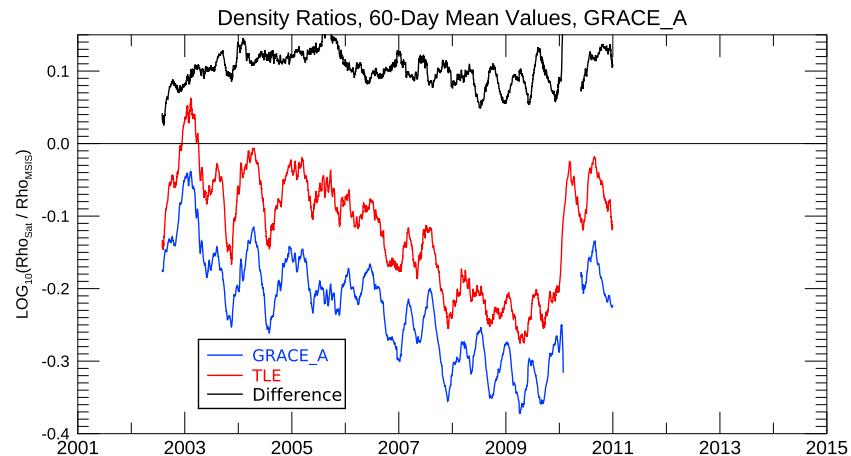
Figure 4. (blue) Natural log of the ratio of GRACE A densities with respect to MSIS. (red) Corresponding TLE log-ratios, interpolated to the altitude of CHAMP. (black) The difference between the TLE and GRACE A log-ratios. GRACE A = Gravity Recovery and Climate Experiment A; TLE = two-line element.

apogee) in 2002 to 310–450 km in 2009. All options in MSIS model were "on," including the use of the 3-hr ap indices, rather than a daily Ap index.

Both data sets have been smoothed by a 60-day running average to remove short-term variability. Even though the red line represents the TLE global averages and the blue line has only values along the CHAMP orbit, overall, there is excellent agreement between them, including the sudden increase at the start of 2010, just before the CHAMP data end. Short-term variations in the graphed values are apparent, as well as the long-term trend from 2006 to 2009 when the solar cycle and thermosphere reached record-low levels (Emmert et al., 2010, 2014), and the measured densities decreased more than predicted by the MSIS model. The difference between these two results is shown with the black line. Since a logarithmic scale is used, this difference represents their ratio, in which a difference of zero corresponds to a 1:1 ratio. Taking the mean value of the line shown in black indicates that these CHAMP measurements need to be multiplied by 1.12 to match the TLE values. Other than that, the results shown in Figure 3 indicate that these data sets are actually in very good agreement with each other. As mentioned earlier, the source of these CHAMP data are from the supplemental data to the paper by Mehta et al. (2017). The result of this process is a comparison of the densities from CHAMP with the TLE densities obtained from the orbits of 5,000 objects, with the MSIS model serving as an intermediate reference.

A similar comparison was done for the densities from the GRACE A satellite, with the results shown in Figure 4. As before, the red line shows the TLE ratios, and the blue line represents the ratios obtained with the neutral density measurements on GRACE A. The altitude of GRACE A varied from a range of about 470–540 to 455–510 km. It was found that the differences between the GRACE A and TLE densities are greater than with CHAMP, particularly before 2006, as shown with the black line. From these results it was found that, in order to agree with TLE global average densities, the GRACE A densities need to be multiplied by 1.25 prior to 2004, 1.33 in 2004 and 2005, and multiplied by 1.24 in 2006 and later. While there are also data from the second, GRACE B satellite, its orbit is so close to GRACE A that very little additional information can be gained from their use. Initially, GRACE A was ahead of GRACE B in their orbit, and in December 2005, their positions were reversed. At the same time, the leading and trailing sides of both satellites were reversed, so that instrument transmitters/receivers would point toward each other. These changes in orientation are assumed to be the cause of the different density corrections seen at the start of 2006.

Moving on to the GOCE data, Figure 5 shows the results of the comparison using the GOCE density measurements, using the same format and color coding as in Figures 3 and 4. The GOCE satellite orbited at an altitude initially in the range of ≈255–295 km in 2009, decreasing to 220–280 km before reentry in 2013. According to these results, the GOCE data needed to be multiplied by 1.12 in order to agree with TLE global average densities. A noticeable feature of Figures 3 to 5 is that the amplitudes of the red lines are not the same, which is because these density ratios vary with altitude.
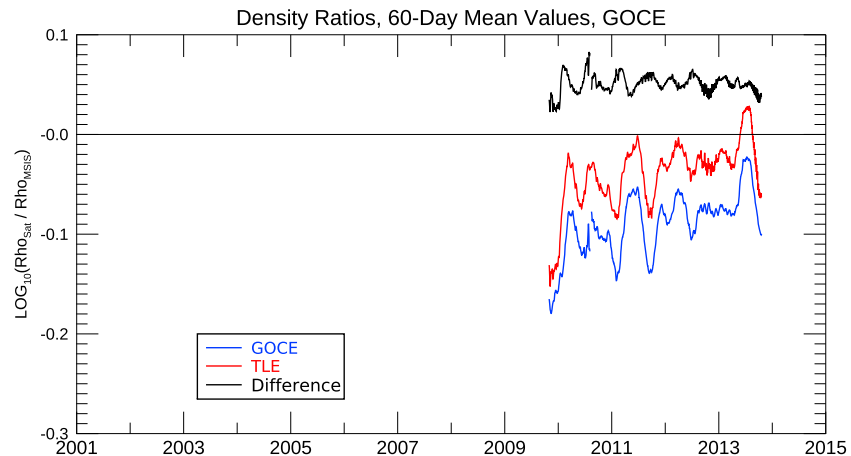
Figure 5. (blue) Natural log of the ratio of GOCE densities with respect to MSIS. (red) Corresponding TLE log-ratios, interpolated to the altitude of CHAMP. (black) The difference between the TLE and GOCE log-ratios. GOCE = Gravity field and Ocean Circulation Explorer; TLE = two-line element.

Unfortunately, the same comparison cannot be made in exactly the same manner for the Swarm density measurements, since the TLE database ends just as the Swarm mission is beginning. In order to perform a similar calibration check on the Swarm data a substitute was derived for the TLE density ratios. This proxy was created by regressing the TLE ratios onto measurements from the SABER instrument.

Figure 6 shows the results of the proxy substitution, applied to the neutral density measurements from Swarm A. As in the earlier graphs, the red line shows the measured/model TLE density ratios. The green line shows the result of fitting this line with the CO_2 and NO radiated power measured with the SABER instrument. This fitting was done separately for the ten different altitudes in the database. The results that are graphed are with both the red and green lines are interpolated to the initial altitude of the Swarm A satellite, then the green line is interpolated to the actual altitude of Swarm A after 2014, which was in the range of $\approx 460-490$ km.

The TLE and SABER measurements were smoothed using a 365-day moving average prior to the fitting, which basically acts as a low-pass filter. While the MSIS model captures the average SAO well, there are interannual variations of the combined SAO and annual oscillation that are not reproduced as well by MSIS. These differences between the modeled and actual interannual variations are the cause of the semi-periodic fluctuations that are seen in Figures 3 to 5. On the other hand, the SABER measurements of the CO_2 emissions are roughly in phase with the thermosphere oscillations, as will be seen shortly. The regression fit of the TLE data with the

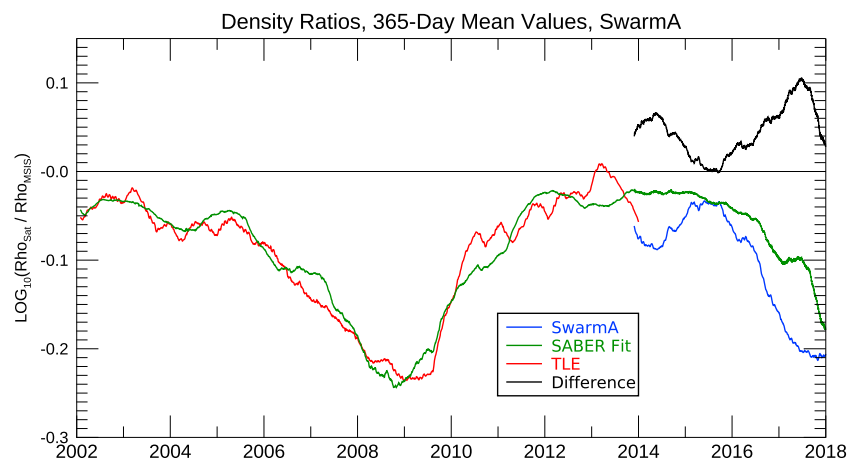**Figure 6.** (blue) Natural log of the ratio of Swarm A densities with respect to MSIS. (red) TLE log-ratios, interpolated to the initial altitude of Swarm A. (green) Result from fitting the red line to the SABER global NO and CO_2 emissions. (black) The difference between the green and blue lines. SABER = Sounding of the Atmosphere using Broadband Emission Radiometry; TLE = two-line element.
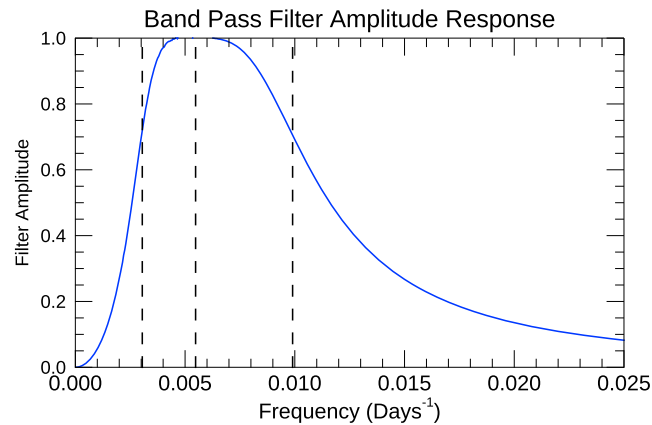
Figure 7. Amplitude response of the digital band-pass filter.

SABER measurements did not work very well without the smoothing. The equation that was used in the fit was

$$\text{Ratio} = a + b \, \text{NO} + c \, \text{CO}_2 + d \, \text{NO}^f + e \, \text{CO}_2{}^g \tag{1}$$

While the data that were used for the fitting do not extend beyond the start of 2014, the SABER measurements continue onward, as indicated with the green line, serving as a substitute for the TLE density ratio. The blue line in Figure 6 shows the ratio obtained from the densities measured with the Swarm A spacecraft (and simultaneous MSIS calculations), as in the prior figures, but with the 365-day smoothing. The black line shows the difference from the green line, as before. Using the mean value of this difference, it was found that multiplying the Swarm A density measurements by 1.08 brings them in agreement with the TLE ratio proxy. The same result was found for the densities from the Swarm C spacecraft, at the same altitude as Swarm A. For Swarm B, at an altitude of 510–540 km, a correction factor of 1.10 is used. As the ratio proxy does not have the same accuracy and temporal resolution as the original TLE ratios, there is greater uncertainty in these adjustment factors for the Swarm spacecraft.

5. Measuring the Semiannual Variations

The next step is to derive the amplitudes of the combined, annual and semiannual variations using the density data from the various satellites. As previously shown by Weimer et al. (2016), this can be done by using the MSIS model if the flags that control these variations are turned off, and then comparing the density computed by MSIS along each satellite's orbit with the measured densities. One measure of the level of the variability is obtained by computing the percent change in atomic oxygen that is needed in MSIS in order match the observed values. Alternatively, the ratio of the measured and modeled densities can be used, although this ratio varies with altitude.

Either way, one problem with this process is that the result includes the long-term variations produced by the MSIS model during the course of the solar cycle, as shown in Figures 2 to 6. Additionally, within each orbit and from day to day there is much variability, appearing as noise when graphed over long time scales. To remove both the high- and low-frequency (solar cycle) components from the results, digital band-pass filtering has been applied. Prior to this filtering the density results were reduced to daily averages.

Figure 7 shows the amplitude response curve of the filter that was used. Although forward and reverse Fourier transforms were actually used in this filtering, the response curve was calculated for a second-order digital band-pass filter, using the techniques described by Stanley et al. (1984) for an "infinite impulse response" filter. The peak amplitude of this filter, indicated with the centermost vertical dashed line in the figure, corresponds to two complete cycles per year. The width of the pass band is set at 1.25 times this frequency, found by experimentation to achieve the desired rejection of the high and low frequencies. The other two dashed lines indicate where the amplitude of this filter is reduced to a factor of $1/\sqrt{2}$, a traditional indicator of the "roll-over" frequency (Stanley et al., 1984).
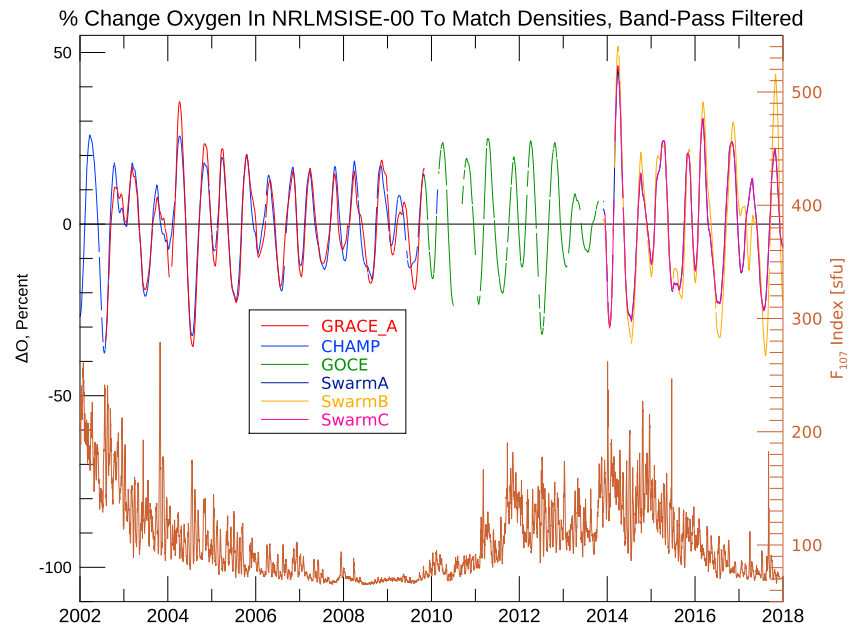
Figure 8. Percentage change in atomic oxygen needed in the MSIS model to match the measured densities, after band-pass filtering. Each line color represents the results from a different satellite, indicated within the legend in the box. The brown line at the bottom shows the solar $F_{10.7}$ index. GRACE A = Gravity Recovery and Climate Experiment A; CHAMP = Challenging Minisatellite Payload; GOCE = Gravity field and Ocean Circulation Explorer.

Figure 8 shows the percentage change in atomic oxygen needed in the MSIS model (with built-in annual and semiannual terms turned off) that would account for the observed density changes, after use of the band-pass filtering. Initially, these values were derived for every available density measurement, with the MSIS model evaluated at each satellite's exact coordinates, including altitude. Averaging was then used to condense these data to 1-day sample rates, and these data were strung together into one continuous time series prior to filtering. Different line colors are used for each satellite, as indicated with the legend included in the box. Gaps in some lines indicate where data were missing, although filled in by interpolation prior to filtering. The results from all three Swarm spacecraft are included, and these lines were drawn in the order A, B, and C. As a result, the line for Swarm A is mostly covered by the line for Swarm C. Similarly, the results from CHAMP and GRACE A mostly overlap each other. Originally the CHAMP and GRACE A results had a good agreement with the GOCE data where they overlapped in time. The lines that are drawn for CHAMP, GOCE, and Swarm A are from the result of combining together only these three data sets prior to the filtering. The lines drawn for the other satellites are taken from other combinations, such as GRACE A, GOCE, and Swarm C, prior to the filtering. For comparison, the brown line at the bottom shows the solar $F_{10.7}$ index during the same time period.

The use of atomic oxygen is based on the reasoning that this species would be the one that is most likely to vary (Emmert, 2015a; Fuller-Rowell, 1998). It is possible that these seasonal variations may not be composed of entirely atomic oxygen, so these results should be considered only as the equivalent change in oxygen content. Additionally, the exospheric temperatures also vary with the SAOs, roughly in phase with the oxygen. In the MSIS model the amplitude of these temperature changes is approximately $13°K$.

Figure 9 shows the ratios between the satellite density measurements and the MSIS model, after application of the same band-pass filtering. The base 10 logarithm of the measured/modeled ratios are shown, after mapping all quantities to an altitude of 400 km. The line colors are the same as in Figure 8. In both Figures 8 and 9 it is seen in the results from the GOCE satellite (green line) that the oscillatory signal has a much lower amplitude in 2013. At this time the altitude of GOCE was rapidly decreasing, with perigee dipping below 230 km, as it neared reentry. This lower altitude appears to be related to the lower amplitude of the measured oscillations.

6. Correlations With the SABER Measurements

Now that the seasonal density variations have been obtained, we can compare the results with the CO_2 and NO emissions measured with the SABER instrument. Figure 10 shows these emissions after processing through
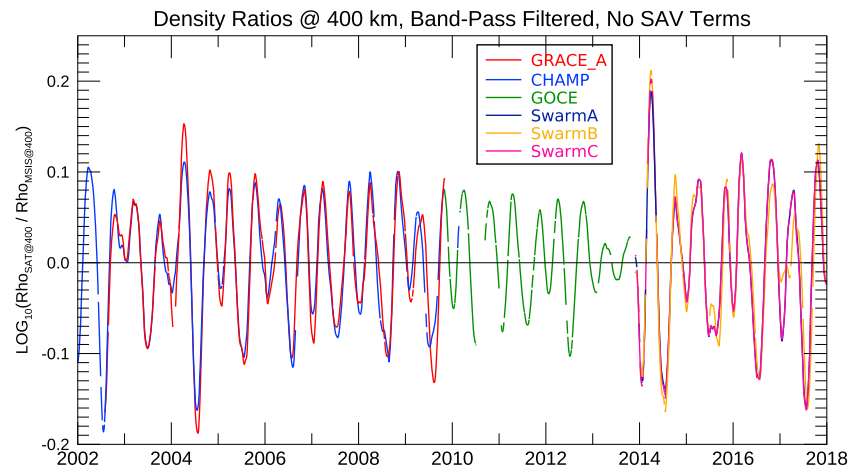
Figure 9. Logarithm of the ratio of the measured and MSIS model densities, both mapped to 400 km, after band-pass filtering. Each line color represents the results from a different satellite, indicated within the legend in the box. GRACE A = Gravity Recovery and Climate Experiment A; CHAMP = Challenging Minisatellite Payload; GOCE = Gravity field and Ocean Circulation Explorer; SAV = semiannual variation.

the same band-pass filter used for the density measurements. Right away, it is obvious that the CO_2 variations have features in common with the density variations graphed in Figures 8 and 9, particularly during the major minimums seen near the middle of each year. These common features are not too surprising. As explained by Mlynczak et al. (2010), atomic oxygen influences the chain of collisional processes that lead to the infrared radiative cooling of the atmosphere by CO_2 and NO. Thermospheric temperatures also influence the intensity of the radiative emissions and the neutral density.

In order to compare the SABER measurements with the measured density changes, a single-valued, continuous function of time is needed. As was done for Figures 8 and 9, the data from the CHAMP, GOCE, and Swarm A were joined together, then processed through the band-pass filter. The comparison of the simultaneous results from CHAMP and GRACE A that are shown in these two prior figures is useful for validation purposes, as very similar results are obtained. For this final comparison only one set was needed, so only the CHAMP data were used, as these had less uncertainty about the drag coefficients. Likewise, only the Swarm A data are needed for the final comparisons.

Figure 11 shows the results of least-error fits of the SABER measurements with the derived percentage change in atomic oxygen, like those shown in Figure 8. As done before, any data gaps in the 1-day mean values were filled by interpolation prior to the filtering. In the Figure 11 graphs these interpolated values remain in place,
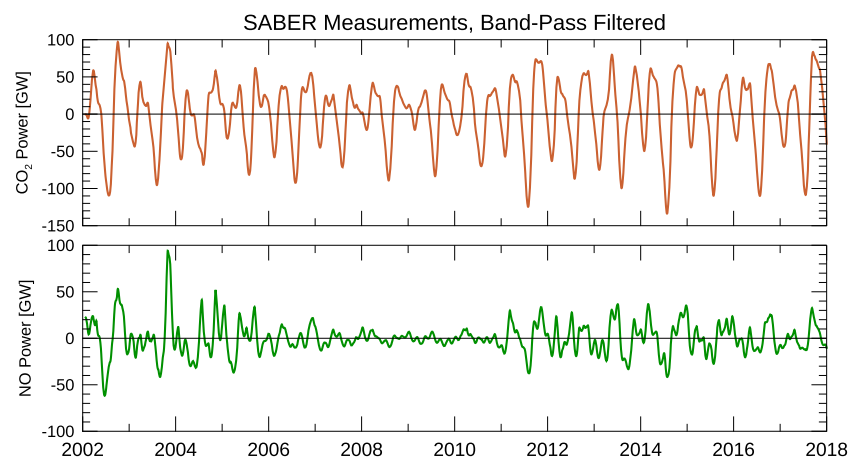

Figure 10. The measured CO_2 and NO emissions, after band-pass filtering. SABER = Sounding of the Atmosphere using Broadband Emission Radiometry.
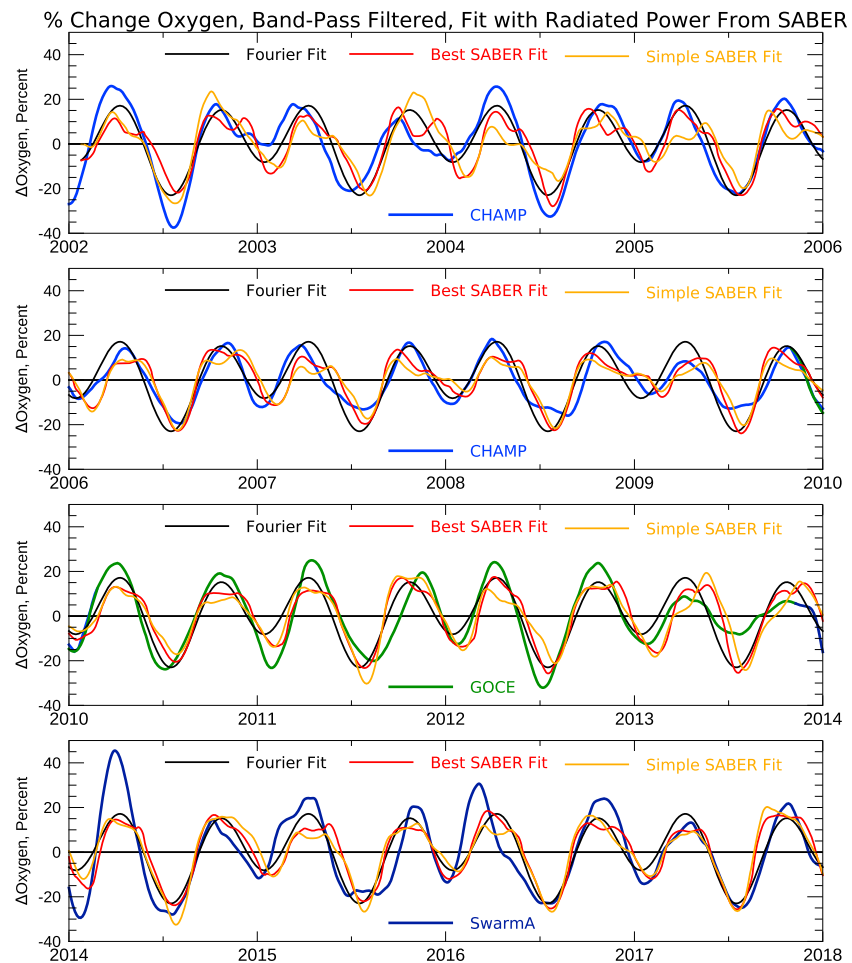
Figure 11. Result of fitting the semiannual variations with SABER measurements. The light-blue, green, and dark-blue lines show the measured semiannual variations from the CHAMP, GOCE, and Swarm A satellites. The graph shows the percentage change in atomic oxygen needed in the MSIS model to match the measured densities, after band-pass filtering. The orange line shows a simple fit using only CO_2 measurements, and the red line shows the best fit that uses both NO and CO_2 measurements. The black line shows the result of fitting the measurements with a simple Fourier series, a function of time only. Only the results from CHAMP and GOCE, up to 2013, were used in the fits, while the Swarm A results are used for comparison. The 16-year time period has been divided into four rows, as indicated with the dates on each horizontal axis, to improve the resolution. CHAMP = Challenging Minisatellite Payload; GOCE = Gravity field and Ocean Circulation Explorer.

and they were also included in the least-error fits. For greater clarity, the horizontal time scale in Figure 11 has been expanded, with the 16-year time period divided into four sections that each span 4 years, as indicated with the dates indicated below each horizontal axis. The line colorings are the same as before, with the results from the CHAMP, GOCE, and Swarm A satellites represented by light-blue, green, and dark-blue lines respectively.

Superposed on Figure 11 are the results of three least-error fits to the atomic oxygen variations. Only the data from CHAMP and GOCE were used for these fits. The Swarm A data were not used in these fits so that they can be used to check the results, serving as as experimental "control." Since the results obtained from GOCE seem abnormal just before reentry, the data from 2013 were not used in the fitting.

While several different formulas were tested, as illustrated with the orange line in Figure 11, even the most simple fit produces a decent match. This was a linear fit using only the CO_2 emissions:

$$\Delta O = a + b\, CO_{2BP} \tag{2}$$

The BP subscript refers to the CO_2 data that had passed through a band-pass digital filter, shown in Figure 10. The values of a and b are included in Table 1. This simple equation correlates with the CHAMP and GOCE

Table 1
Results From Fitting the Atomic Oxygen Variations With Equations (2)–(5)

Equation	a	b	c	d	e	Correlation C/G	Correlation Swarm A	Std. dev. C/G	Std. dev. Swarm A
(2)	−0.0288	0.243				0.735	0.769	9.36	10.9
(3)	0.00695	0.310	−.300			0.801	0.790	8.27	10.4
(4)	−0.466	0.712	−0.461	0.791	0.852	0.806	0.799	8.17	10.3
(5)	0.0882	2.82	6.93	−7.68	−13.6	0.888	0.859	6.36	8.98

Note. Correlation with CHAMP and GOCE (C/G) results and the standard deviation are included, as well as the correlation and standard deviation with Swarm A. CHAMP = Challenging Minisatellite Payload; GOCE = Gravity field and Ocean Circulation Explorer.

results with a coefficient of 0.735, and the standard deviation is 9.4. The comparison with Swarm A actually produces a higher correlation, 0.769, although the standard deviation is greater at 10.0. Close examination of the graph shows some differences between the data (light blue) and this fit (orange) near the end of 2003, when there was unusually high levels of solar activity that may have boosted the CO_2 power levels.

Including the NO in the fit helps to compensate for solar activity, using the equation:

$$\Delta O = a + b \, CO_{2BP} + c \, NO_{BP} \tag{3}$$

The constants a through c, also listed in Table 1, were determined by a multiple linear regression fit. The role of the nitric oxide (NO) in this fit equation is basically to compensate for variations in the CO_2 emissions that are responding to the heating of the thermosphere, rather than the semiannual variations. The results of this fit have a correlation of 0.801 with the CHAMP and GOCE data, and a standard deviation of 8.27, slightly better than the more simple fit. Comparing the results from (3) with the variations derived from the Swarm A data, the correlation was 0.790, and the standard deviation was 10.4.

A variation of (3) was tested that applies noninteger exponents to the filtered CO_2 and NO emissions:

$$\Delta O = a + b \, \mathrm{sgn}\left(CO_{2BP}\right) \, |CO_{2BP}|^d + c \, \mathrm{sgn}\left(NO_{BP}\right) \, |NO_{BP}|^e \tag{4}$$

The result of the multiple linear regression fit is shown with the red line in Figure 11, as "the best SABER fit," with the values a through e listed in Table 1. The d and e exponents were optimized by repeating the regression with different values, controlled by the "downhill simplex method" (Press et al., 1986) until the error was minimized. The results from (4) were just barely better than (3), having higher correlations and lower standard deviations in Table 1 in only the third decimal place, scarcely significant. Visually, the result from this fit matches the variations seen in the Swarm A data fairly well, except for the winter peaks near the beginning of 2014 and 2016.

To complete these tests, the black line in Figure 11 shows the results of fitting the atomic oxygen variations with just a simple Fourier series function of time:

$$\Delta O(t) = a + b \, \sin \Theta + c \, \cos \Theta + d \, \sin 2\Theta + e \, \cos 2\Theta \tag{5}$$

where $\Theta = t * 2\pi/365.25$ and t is the time in days after 1 January 2004. The values of the constants a through e that were found using a multiple linear regression fit are listed in Table 1. The results of this fit have a correlation of 0.89 with the CHAMP and GOCE data, and a standard deviation of 6.36. The correlation with the Swarm data was 0.86 and a standard deviation of 8.98. This simple Fourier series actually has the better results. Adding additional terms in (5), up to 4Θ, did not substantially improve the correlations.

The logarithm of the ratio of the measured and MSIS model densities, as shown in Figure 9, has also been fit using equations (2) to (5), with the results included in Table 2. Other than a difference in the vertical scale, the results did not look much different from those shown in Figure 11, so the graph is not included here.

7. Discussion

The results shown in Figures 8, 9, and 11 demonstrate the complexity of the thermosphere's oscillations that result from the combined effects of the annual oscillations and SAOs, showing the variations in both amplitude and phase timing. One feature seen in Figure 8 is that the amplitudes of the semiannual and annual

Table 2
Results From Fitting the Density Ratios With Equations (2)–(5)

Equation	a	b	c	d	e	Correlation C/G	Correlation Swarm A	Std. dev. C/G	Std. dev. Swarm A
(2)	−0.000269	0.00106				0.730	0.824	0.0416	0.0465
(3)	−0.000107	0.00137	−0.00136			0.800	0.839	0.0365	0.0444
(4)	−0.00228	0.00294	−0.00330	0.810	0.725	0.807	0.840	0.0360	0.0450
(5)	0.000243	0.0126	0.0343	−0.0337	−0.0605	0.909	0.899	0.0254	0.0386

Note. Correlation with CHAMP and GOCE (C/G) results and the standard deviation are included, as well as the correlation and standard deviation with Swarm A. CHAMP = Challenging Minisatellite Payload; GOCE = Gravity field and Ocean Circulation Explorer.

oscillations appear to vary in proportion to solar activity, as previously noted by Emmert and Picone (2010) and Bowman et al. (2008). This relationship is particularly evident during the deep solar minimum in the years 2007 through 2009, where the amplitudes of the oscillations are reduced.

Despite this variability, measurements of the radiative emissions from CO_2 correlate with these changes quite well through the use of equations (2), (3), or (4). The midyear minimums are very pronounced in both the density measurements and the SABER measurements of the CO_2 emissions, as seen in the figures. In the satellite density measurements the lowest points were found to occur as early as 29 June 2003 and as late as 26 August 2008. Surprisingly, the minimums in the best fit results from the SABER measurements (equation (3)) fell within a more narrow time window, all clustered between 17 and 31 July. Interestingly, the lowest observed CO_2 emissions in 2008 and 2009 occur simultaneously with the lowest densities measured in the last solar minimum, coinciding with the minimum of the SAO.

The oscillations have two peaks during the year, with one occurring in the spring between 6 March and 21 April, and another maximum in the fall between 3 October and 17 November. The spring maximum tends to peak at a higher level of derived atomic oxygen variations (and density ratios) than at the fall maximum, although not always. Between the fall and spring peaks there is often another minimum in these values, usually occurring between 4 January and 1 February. In some years these more minor peaks and valleys are almost absent in the measured density variations, such as in 2003 and 2009, and their amplitudes have a wide variation. The results from fitting the SABER measurements do not match the minor density oscillations quite as well as they do at the summer minimums, although they do have characteristics that are in general agreement. Emmert and Picone (2010) have examined this "interannual variability" in much greater detail, through the use of the TLE database spanning the years 1967–2007.

Surprisingly, the fit that uses a simple Fourier series resulted in better correlations with the measured variations than the fits using the SABER measurements, even though the timings and amplitudes of the minimum and maximum values are unvarying. The deeper summer minimums in this fit occur on 17 and 18 July (shifting due to leap years), the winter minimum is on 14 and 15 January, the spring maximum falls on 9 and 10 April, and the fall maximum is 23 and 24 October.

There is very strong evidence that future, real-time measurements of optical emissions from the thermosphere could be a valuable resource for monitoring and forecasting of the global density fluctuations occurring during geomagnetic storms. In such cases the emissions, from nitric oxide in particular, have a strong correlation with total ionospheric heating, the thermosphere's temperature, and subsequent cooling rate (Knipp et al., 2017; Weimer et al., 2015, 2016). As discussed by Mlynczak et al. (2018), a customized group of satellites and instrumentation could be used for nowcast purposes.

Even though our results found that the simple Fourier series worked best for predicting the timing of the semiannual variations, for future observations of the progression of the semiannual variation in real time, there may yet be some use for such measurements on special-purpose satellites. Note that smoothing of data through the use of moving-box averages would be difficult to apply in such situations, as the averages at the end of the time series would require measurements at future times, unless edge truncation is used. The slightly more complicated digital band-pass filtering of a time series does not require data from future times so is more appropriate.

8. Summary

This paper presents the results of an investigation of the amplitudes and timings of the combined, annual, and semiannual variations of thermospheric neutral density and a comparison of these density variations with measurements of the infrared emissions from carbon dioxide and nitric oxide in the thermosphere. The density values were obtained from measurements of the atmospheric drag experienced by the CHAMP, GRACE A, GOCE, and three Swarm satellites, while the optical emissions were measured with the SABER instrument on the TIMED satellite.

In order to make sure that the density measurements were in agreement with each other, they were compared against a long-term database in which neutral densities were derived, as a function of altitude between 200 and 600 km, from the orbital elements of approximately 5,000 objects (Emmert, 2009, 2015b). This TLE database included the ratios of these measurements to the global average calculated with the MSIS model, as a function of time. By comparing these ratios with those obtained from the six satellites (four missions) that we used, small adjustments to the original density values were obtained. Measurements from the SABER instrument were fit to the TLE data that end before 2014 to serve as a proxy substitute during the time period of the Swarm mission.

With these adjustments made, density measurements were compared with the MSIS model output at all times. With the optional annual and semiannual terms in the MSIS model turned off, the comparison reveals how much the density changes over time due to these seasonal variations. These results show that over the 16-year time period spanned by our data, these fluctuations have substantial changes in amplitude from one year to the next, as previously shown by Emmert and Picone (2010). This range of variability makes these density variations difficult to precisely predict with any empirical model that uses fixed amplitudes and periodicity.

This variability was shown here with graphs of the percentage change in atomic oxygen that would produce the same density swings in the output of the MSIS model. These results show the percentage change in atomic oxygen that is needed to produce the observed variability. Actual, in situ measurements of the composition would be needed to confirm that fluctuations in the level of atomic oxygen are entirely responsible for the seasonal variations. Another comparison used the logarithm of the ratio between the measured and MSIS densities. We note that these graphs show global averages, while in reality, the seasonal oscillations have a well-known latitudinal dependance (Bowman et al., 2008; Emmert & Picone, 2010; Jones et al., 2018). Even so, the latitudinal dependancies are modulated by the amplitude of the signals that are shown.

The measurements from the SABER instrument were fit to these observed variations in order to determine how well they correlate with the thermosphere oscillations and to determine if such emissions could be used as a monitoring tool. All quantities were frequency band-pass filtered prior to these fits. The formula producing the best fit included the nitric oxide emissions, which help to compensate for the effects of geomagnetic activity. While the results from this fitting exercise were not perfect, there were reasonably good correlations (0.80), particularly when compared with the measurements from the Swarm A spacecraft, which were not included in the fitting. In general, even the most simple fit that used only the CO_2 emissions, with band-pass filtering, tends to match the amplitudes of the more variable density maximums and minimums. On the other hand, these fits did not do any better in matching the measured oscillations than a simple Fourier series function of time, contrary to original expectations. Obviously, there are other variables in action that influence the magnitudes of these seasonal oscillations that presently defy accurate predictability. The role of all such unknown factors may someday become known, most likely through the use of improved numerical simulations; the optical radiation from the thermosphere will undoubtedly be a critical quantity needed for these calculations.

Acronyms

CHAMP Challenging Minisatellite Payload satellite and (GRACE)
GRACE Gravity Recovery and Climate Experiment satellite
GOCE Gravity field and Ocean Circulation Explorer
MSIS Abbreviation for NRLMSISE-00
NRLMSISE-00 NRL Mass Spectrometer and Incoherent Scatter radar Extended model 2000
SABER Sounding of the Atmosphere using Broadband Emission Radiometry instrument
SAO semiannual oscillation
SAV semiannual variation, another term for SAO
TIMED Thermosphere Ionosphere Mesosphere Energetics and Dynamics satellite

References

Astafyeva, E., Zakharenkova, I., Huba, J. D., Doornbos, E., & van den IJssel, J. (2017). Global ionospheric and thermospheric effects of the June 2015 geomagnetic disturbances: Multi-instrumental observations and modeling. *Journal of Geophysical Research: Space Physics*, *112*, 11,716—11,742. https://doi.org/10.1002/2017JA024174

Bowman, B. R., Tobiska, W. K., & Kendra, M. J. (2008). The thermospheric semiannual density response to solar EUV heating. *Journal of Atmospheric and Solar - Terrestrial Physics*, *70*, 1482–1496. https://doi.org/10.1016/j.jastp.2008.04.020

Bruinsma, S., Tamagnan, D., & Biancale, R. (2004). Atmospheric densities derived from CHAMP/STAR accelerometer observations. *Planetary and Space Science*, *52*, 297–312.

Doornbos, E. (2012). *Thermospheric density and wind determination from satellite dynamics*. Berlin: Springer. https://doi.org/10.1007/978-3-642-25129-0

Doornbos, E. (2016). GOCE+ Theme 3: Air density and wind retrieval using GOCE, data set user manual (*Technical Report ESA AO/1-6367/10/NL/AF*). Delft, NL: European Space Agency. Retrieved from https://earth.esa.int/documents/10174/679909/GOCEPlus_Theme_3_Dataset_User_Manual

Doornbos, E., Bruinsma, S., Fritsche, B., Koppenwallner, G., Visser, P., van den IJssel, J., & de Teixeira de Encarnacao, J. (2014). GOCE+ Theme 3: Air density and wind retrieval using GOCE, final report (*Technical Report ESA 4000102847/NL/EL*). Delft, NL: European Space Agency. Retrieved from https://earth.esa.int/documents/10174/679909/GOCEPlus_Theme_3_FinalReport_ATBD_Validation_Appendices

Emmert, J. T. (2009). A long-term data set of globally averaged thermospheric total mass density. *Journal of Geophysical Research*, *114*, A06315. https://doi.org/10.1029/2009JA014102

Emmert, J. T. (2015a). Thermospheric mass density: A review. *Advances in Space Research*, *56*(5), 773–824. https://doi.org/10.1016/j.asr.2015.05.038

Emmert, J. T. (2015b). Altitude and solar activity dependence of 1967–2005 thermospheric density trends derived from orbital drag. *Journal of Geophysical Research: Space Physics*, *120*, 2940–2950. https://doi.org/10.1002/2015JA021047

Emmert, J. T., Lean, J. L., & Picone, J. M. (2010). Record-low thermospheric density during the 2008 solar minimum. *Geophysical Research Letters*, *37*, L12102. https://doi.org/10.1029/2010GL043671

Emmert, J. T., McDonald, S. E., Drob, D. P., Meier, R. R., Lean, J. L., & Picone, J. M. (2014). Attribution of interminima changes in the global thermosphere and ionosphere. *Journal of Geophysical Research: Space Physics*, *119*, 6657–6688. https://doi.org/10.1002/2013JA019484

Emmert, J. T., & Picone, J. M. (2010). Climatology of globally averaged thermospheric mass density. *Journal of Geophysical Research*, *115*, A09326. https://doi.org/10.1029/2010JA015298

Fuller-Rowell, T. J. (1998). The "thermospheric spoon": A mechanism for the semiannual density variation. *Journal of Geophysical Research*, *103*(A3), 3951–3956. https://doi.org/10.1029/97JA03335

Haagmans, R., Bock, R., & Rider, H. (2013). Swarm: ESA's magnetic field mission (*Tech. Rep. BR-302*): European Space Agency. Retrieved from https://esamultimedia.esa.int/multimedia/publications/BR-302/

Hedin, A. E. (1991). Extension of the MSIS thermosphere model into the middle and lower atmosphere. *Journal of Geophysical Research*, *96*, 1159–1172.

Jones, M., Emmert, J. T., Drob, D. P., Picone, J. M., & Meier, R. R. (2018). Origins of the thermosphere-ionosphere semiannual oscillation: Reformulating the "thermospheric spoon" mechanism. *Journal of Geophysical Research: Space Physics*, *123*, 931–954. https://doi.org/10.1002/2017JA024861

Knipp, D. J., Pette, D. V., Kilcommons, L. M., Isaacs, T. L., Cruz, A. A., Mlynczak, M. G., et al. (2017). Thermospheric nitric oxide response to shock-led storms. *Space Weather*, *15*, 325–342. https://doi.org/10.1002/2016SW001567

March, G., Doornbos, E., & Visser, P. (2018). High-fidelity geometry models for improving the consistency of champ, grace, goce and swarm thermospheric density data sets. *Advances in Space Research*. https://doi.org/10.1016/j.asr.2018.07.009

Mehta, P. M., Walker, A. C., Sutton, E. K., & Godinez, H. C. (2017). New density estimates derived using accelerometers on board the champ and grace satellites. *Space Weather*, *15*, 558–576. https://doi.org/10.1002/2016SW001562

Mlynczak, M. G., Hunt, L. A., Marshall, T., Martin-Torres, F. J., Mertens, C. J., Russell, J. M., et al. (2010). Observations of infrared radiative cooling in the thermosphere on daily to multiyear timescales from the TIMED/SABER instrument. *J. Geophys. Res.*, *115*, A03309. https://doi.org/10.1029/2009JA014713

Mlynczak, M. G., Knipp, D. J., Hunt, L. A., Gaebler, J., Matsuo, T., Kilcommons, L. M., & Young, C. L. (2018). Space-based sentinels for measurement of infrared cooling in the thermosphere for space weather nowcasting and forecasting. *Space Weather*, *16*, 363–375. https://doi.org/10.1002/2017SW001757

Mlynczak, M. G., Martin-Torres, F. J., Crowley, G., Kratz, D. P., Funke, B., Lu, G., et al. (2005). Energy transport in the thermosphere during the solar storms of April 2002. *Journal of Geophysical Research*, *110*, A12S25. https://doi.org/10.1029/2005JA011141

Mlynczak, M. G., Martin-Torres, F. J., Mertens, C. J., Marshall, B. T., Thompson, R. E., Kozyra, J. U., et al. (2008). Solar-terrestrial coupling evidenced by periodic behavior in geomagnetic indexes and the infrared energy budget of the thermosphere. *Geophysical Research Letters*, *35*, L05808. https://doi.org/10.1029/2007GL032620

Paetzold, H. K., & Zschörner, H. (1961). An annual and a semiannual variation of the upper air density. *Pure and Applied Geophysics*, *48*, 85–92.

Picone, J., Hedin, A., Drob, D., & Aikin, A. (2002). NRLMSISE-00 empirical model of the atmosphere: Statistical comparisons and scientific issues. *Journal of Geophysical Research*, *107*(A12), 1468. https://doi.org/10.1029/2002JA009430

Pilinski, M. D., Argrow, B. M., & Palo, S. E. (2011). Drag coefficients of satellites with concave geometries: Comparing models and observations. *Journal of Spacecraft and Rockets*, *48*(2), 312–325. https://doi.org/10.2514/1.50915

Press, W. H., Flannery, B. P., Teukolsky, S. A., & Vetterling, W. T. (1986). *Numerical recipes: The art of scientific computing*. New York: Cambridge University Press.

Stanley, W. D., Dougherty, G. R., & Dougherty, R. (1984). *Digital Signal Processing* (2nd ed., 514 pp.). Reston, VA: Reston Publishing Co.

Sutton, E. K. (2016). Interhemispheric transport of light neutral species in the thermosphere. *Geophysical Research Letters*, *43*, 12,325–12,332. https://doi.org/10.1002/2016GL071679

Tapley, B. D., Watkins, S. B. M., & Reigber, C. (2004). The gravity recovery and climate experiment: Mission overview and early results. *Geophysical Research Letters*, *31*, L09607. https://doi.org/10.1029/2004GL019929

Weimer, D. R., Mlynczak, M. G., & Hunt, L. A. (2016). Intercalibration of neutral density measurements for mapping the thermosphere. *Journal of Geophysical Research: Space Physics*, *121*, 5975–5990. https://doi.org/10.1002/2016JA022691

Weimer, D. R., Mlynczak, M. G., Hunt, L. A., & Tobiska, W. K. (2015). High correlations between temperature and nitric oxide in the thermosphere. *Journal of Geophysical Research: Space Physics*, *120*, 1–12. https://doi.org/10.1002/2015JA021461